Available online at www.sciencedirect.com
SCIENCE DIRECT®
International Journal of Heat and Mass Transfer 48 (2005) 2385–2396
International Journal of HEAT and MASS TRANSFER
www.elsevier.com/locate/ijhmt

Dendritic growth in Al–Si alloys during brazing. Part 2: Computational modeling

D.P. Sekulic [a,*], P.K. Galenko [b], M.D. Krivilyov [c], L. Walker [d], F. Gao [e]

[a] University of Kentucky Center for Manufacturing, College of Engineering, University of Kentucky, 521 CRMS Building, Lexington, KY 40506-0108, USA
[b] Institute of Space Simulation, German Aerospace Center, Cologne 51170, Germany
[c] Department of Metallurgy and Materials Engineering, KU Leuven, Heverlee 3001, Belgium
[d] High Temperature Materials Laboratory, Oak Ridge National Laboratory, Oak Ridge, TN 37831, USA
[e] Collaborative Research Center for Advanced Science and Technology, Osaka University, Osaka 565-0871, Japan

Received 29 March 2004; received in revised form 25 January 2005
Available online 7 April 2005

Abstract

The computational heat and mass transfer modeling approach presented in this paper emphasizes the influence of undercoolings on dendrite structure formations of the alpha phase crystals inherent to advanced phases of an aluminum brazing netshape manufacturing sequence. In the first segment of this work, the empirical evidence involving the outcome of the solidification process and its kinetics was presented. In this paper, simulation of the alpha phase crystal pattern formation is corroborated with empirical findings obtained by utilizing an AA4343/AA3003 brazing sheet exposed to controlled atmosphere brazing (CAB) in ultra-high purity nitrogen.

1. Introduction

The solid solution solidification is a typical phase change phenomenon that takes place in an Al + Si system exposed to a state-of-the-art CAB metal joining. The outcome of the process is a brazed joint structure; see the topology of the related physical domain in Fig. 1, consult also [1]. Solidification microstructures feature both alpha phase and irregular eutectic. An effort is made to simulate an appearance of alpha phase dendrites with fully selected pattern either in rich or scarce dendrite populations, see Fig. 1a and b in Part 1 of these twin papers [2]. The empirical evidence presented indicates a small population of dendrites with fairly well selected pattern if the quench is facilitated from a lower peak brazing temperature [2]. This paper offers computational modeling of this dendrite pattern formation.

Various models have been used to predict defects and patterns in alloy solidification processing [3–5]. In particular, phenomenological two- and three-phase models have been analyzed for porosity formation in aluminum alloys during casting [6].

The modeling of the solidification process performed in this study assumes that the set of relevant material parameters has the values invariant in time and space as indicated in Table 1.

The main research objective is modeling of a macropattern of dendrite solidification microstructures formed at at least two different cooling rates during the

* Corresponding author. Tel.: +1 859 257 2972; fax: +1 859 323 1035.
E-mail address: sekulicd@engr.uky.edu (D.P. Sekulic).

0017-9310/$ - see front matter © 2005 Elsevier Ltd. All rights reserved.
doi:10.1016/j.ijheatmasstransfer.2005.01.036

Nomenclature

C	concentration, dimensionless
D	diffusion coefficient, m^2/s
G	solid fraction, dimensionless
J	solute diffusion flux, s^{-1}
K	curvature, m^{-1}
k	partition coefficient, dimensionless
m_e	liquidus slope, K/at.%
n	unit vector orthogonal to the calculation domain boundary, m
Q	latent heat of solidification, J/m^3
T	temperature, K
t	time, s
x, z	orthogonal coordinates, m
Z	front height or height of perturbation, m

Greek symbols

Γ	capillarity constant, surface tension function, K m
δ	noise amplitude, m
ε	anisotropy parameter, dimensionless
κ	specific heat, J/m^3 K
λ	thermal conductivity, W/m K, stability wavelength, m
μ	kinetic coefficient, m/s K
τ	relaxation time, s

aluminum alloy brazing. In order to simulate the solidification process in brazing of an aluminum alloy, a model of local nonequilibrium solidification [7] (which adopts local nonequilibrium at the solid–liquid interface and inside the bulk phases) has been chosen. Hence, the model describes a sharp transition from a chemical partitioning in solidification to a partitionless solidification at a high undercooling and large crystal growth velocities, which is in good agreement with the existing experimental data [8,9]. Therefore, the following problem is confronted: How an application of a local nonequilibrium model of rapid solidification can be applied to relatively moderate/small undercoolings and moderate/small crystal growth velocities for the conditions characteristic for joint formation during aluminum brazing [10].

2. Physical domain

The physical domain of interest is located in the mushy zone within the joint at the clad–core interface on the melt side, Fig. 1a–c. The bulk of liquid metal is accumulated under the equilibrium membrane [1], representing the joint free surface and exposed to the action of surface tension.

3. System description and mathematical formulation

3.1. Selection of the initial and boundary conditions

The temperature at which the quench starts is determined as follows. From experimental data, several cases were selected, see for example Fig. 1 in Part 1 [2]. The cooling curves were extracted from the CAB thermal processing sequence; see Fig. 3b [2] (note that the quench conditions settings during testing were virtually the same for all experiments with a very small variations at the start of quench as represented by Fig. 3b [2]). So, the onset of quench began at 873 K and 883 K, respectively (the nominal concentrations were in the range as indicated in Table 1, Item 9). These temperatures are the imposed initial temperatures T_0 for respective solidification processes. In addition, using experimental data related to materials' compositions, see Tables 1 and 2 in Part 1 [2], the equilibrium liquidus temperature T_{LE} for hypothesized nominal Si concentrations of the melt (not necessarily the initial concentration) were assessed from the phase diagram. The difference between these two temperatures defines the initial undercooling, i.e., $\Delta T = T_{LE} - T_0$. Assessment of the effective Si concentration was based on the following facts: (1) the initial concentration of the clad in the brazing sheet, (2) diffusion controlled non-equilibrium melting model [11], (3) the presence of intense solid state Si diffusion prior to clad melting [12], (4) the presence of Si diffusion in the joint zone [12], and (4) the presence of core dissolution during the dwell at the peak brazing temperature prior to quench [13]. Consequently, in this study, the Si concentration of the melt within the calculation domain prior to quench was assumed to be in the range from 5.5 at.% up to max 8.5 at.%, see Table 1.

In a space–time region of interest, a hypothetical liquid phase of a binary alloy is assumed to be initially present. The temperatures of the liquid + solid in the mushy zone in actual experiments (either $T_0 = 873$ K or 883 K) are lower than the liquidus temperature for the given set of nominal concentration of the melt and were defined from the equlibrium phase diagram. In other words, $T_{LE} = T_A + m_e C_0$, where $T_A = 933$ K is the equilibrium temperature of solidification for pure Al, C_0 is the nominal concentration of Si in the molten alloy prior to quench, and $m_e = -6.6$ K/at.%. The entity m_e is the slope of the equilibrium liquidus line in the con-

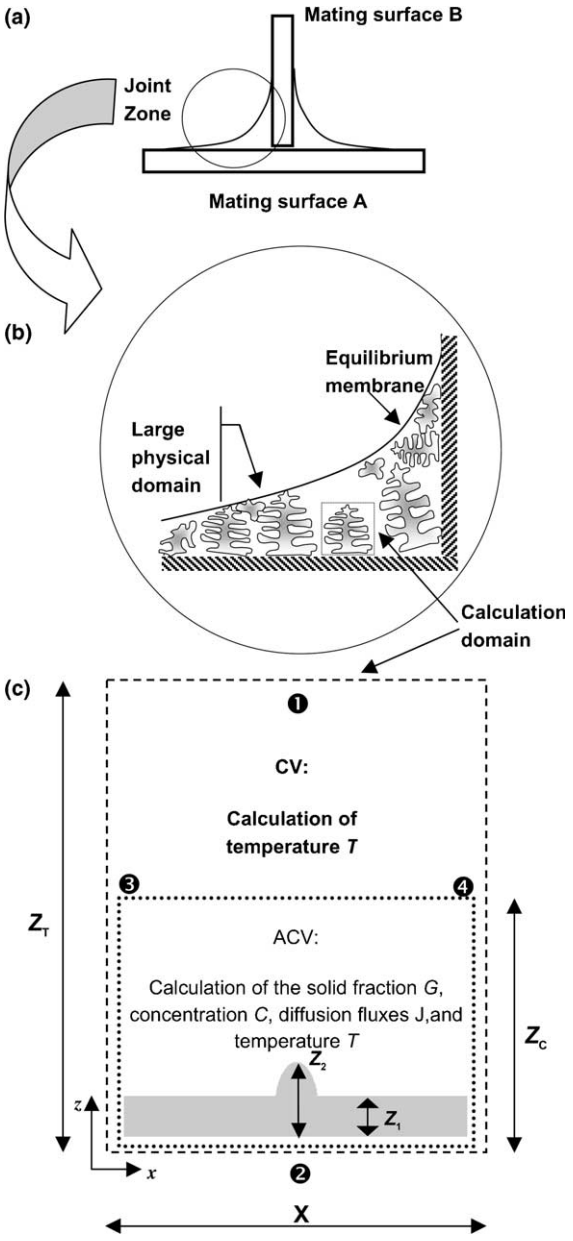

Fig. 1. Physical and calculation domain. Topology of the joint formation vs. calculation domain. (a) The sample; (b) the joint zone; (c) calculation domain. Surfaces 1– 4 are the boundaries of the calculation domain (control volume, CV). CV has the size of $Z_T \times X$. Solute diffusion transfer is calculated within the advancing control volume (ACV) of the size $Z_C \times X$. The height of a smooth front and the unique parabolic perturbation at an initial moment are denoted as Z_1 and Z_2 respectively.

sidered range of concentrations of Si in the phase diagram of the Al–Si alloy, see Table 1. So, in our equivalent liquid model of the melt + solid solution, the liquid is undercooled by $\Delta T_1 = T_{LE} - T_{01} = 4$ K (nominal Si concentration either 8.5 or 6.9 at.%) and $\Delta T_2 = T_{LE} - T_{02} = 14$ K (nominal Si concentration either 5.5 or 6.9 at.%), and the quench starting temperatures are $T_{01} = 883$ K and $T_{02} = 873$ K, respectively.

At the initiation of the modeled sequence, the perturbation is located at the smooth planar front representing the interface between the melt and the solid (close to substrate) phase, boundary 2, Fig. 1c. Therefore, the randomly distributed nucleation sites are generated at that surface. It could be assumed from the experimentally observed microstructure that the volumetric nucleation has been suppressed. The cause for such suppression could be the relatively small initial undercooling, which is followed by a long period of waiting for thermodynamically stable nuclei to be formed. Furthermore, with a relatively high crystal growth rate, bulk liquid is crystallized more rapidly from the substrate.

Let us assume that the origin of the coordinate system is placed at the bottom left corner of the calculated domain, Fig. 1c. In the coordinate system (x, z), initial conditions for the solid fraction G take the following form

$$G = \begin{cases} 1, & \text{if } 0 < z < Z_1, \\ 1, & \text{if } 0 < z < Z_2 - A(x - X/2)^2, \\ 0, & \text{otherwise}, \end{cases} \tag{3.1.1}$$

where the initial configuration of the front is defined by: (a) a smooth front with the height Z_1, (b) a unique parabolic perturbation with the equation $z = Z_2 - A(x - X/2)^2$, where Z_2 is the height of perturbation.

The conditions for the heat removal were established as follows. The boundary conditions of the first kind were assumed at boundaries 1 and 2, see Fig. 1c. Temperature is changing in time in accord with measured experimental cooling rates, Fig. 3b [2], at both top and bottom boundaries 1 and 2, Fig. 1c. It is also assumed that during solidification, the cooling rate is constant until the solidus is reached. At the lateral boundaries 3 and 4 the "cyclic boundary condition" is assumed and it is devised from a requirement of the periodicity of the thermal conditions around the calculation domain. Therefore, the boundary conditions for temperature are described by:

- At the boundaries 1 (i.e., at $z = Z_T$) and 2 (i.e., at $z = 0$), see Fig. 1c,

$$\frac{\partial T(t,x,0)}{\partial t} = \frac{\partial T(t,x,Z_T)}{\partial t} = \text{const.} \tag{3.1.2}$$

- At the boundaries 3 (i.e., at $x = 0$) and 4 ($x = X$),

$$T(t,0,z) = T(t,X,z). \tag{3.1.3}$$

Note that the statement given by Eq. (3.1.2) is fully consistent with imposed boundary conditions of the first kind at the boundaries 1 and 2, i.e. $T(t,x,0) = T(t,x,Z_T) = T(t)$, where $T(t)$ is in accord with corresponding empirical data from Fig. 3b [2], if the

Table 1
Material parameters of the Al–Si alloy used in the modeling

	Parameter	Symbol	Units	Value	Source
1.	Al solidification temperature	T_A	K	933	RB[a] and M[b]
2.	Thermal diffusivity	A	m^2/s	4×10^{-5}	KF[c]
3.	Latent heat of solidification	Q	J/m^3	9×10^{8}	RB[a]
4.	Specific heat	κ	$J/m^3\,K$	2.5×10^{6}	RB[a]
5.	Liquidus slope (Al + Si)	m_e	K/at.%	−6.6	M[b]
6.	Interfacial kinetic coefficient	μ_0	m/s K	0.14	Present work
7.	Capillarity constant	Γ_0	K m	1.1×10^{-7}	RB[a]
8.	Solid–liquid interface tension	γ[d]	J/m^2	0.106	RB[a]
9.	Nominal concentration	C_0	at.%	5.5, 6.9, 8.5	Present work
10.	Interatomic distance	a_0[d]	m	5×10^{-10}	M[b]
11.	Diffusion coefficient	D_L	m^2/s	5.25×10^{-9}	Present work
12.	Diffusion speed in bulk liquid	V_D	m/s	28	Present work
13.	Interface diffusion speed	V_{DI}	m/s	20	Present work
14.	Partition coefficient	k_e	–	0.144	RB[a]
15.	Adiabatic temperature	T_Q[d]	K	360	–
16.	Molar mass of Si	M_{Si}[d]	g/mol	28.06	–
17.	Molar mass of Al	M_{Al}[d]	g/mol	26.97	–

[a] Ref. [25].
[b] Ref. [26].
[c] Ref. [19].
[d] The auxiliary parameters, not used in the modeling directly.

assumption of constant cooling rates is invoked during the period of solidification. In accord with the cooling curves obtained experimentally, the cooling rates were calculated for each of the two experimental conditions (the initial undercoolings of 14 K and 4 K with cooling rates of 7 K/s and 4 K/s, respectively, see Figs. 1 and 3b in [2]).

The boundary conditions for mass transfer were defined as follows. The calculation domain is considered as a region with mass non-penetrating boundaries, i.e., there is the absence of mass transfer at boundaries 1–4 of Fig. 1c (note that modeling starts upon an assumed completion of Si diffusion across the clad–core melt and lasts a very short period of time of the order of magnitude of 10^{-1} s). Note that this does not preclude an eventual presence of an intense Si diffusion prior to quench. This yields

$$\mathbf{n}\cdot\mathbf{J}|_{1-4}=0, \tag{3.1.4}$$

where $\mathbf{n}$ is the unit vector orthogonal to the boundary of the calculated domain and $\mathbf{J}$ is the vector of solute diffusion flux. The empirical evidence does indicate that the mass transfer is present prior to solidification of the melt (see Figs. 4 and 5, [2]), and it is taken into account by assuming the presence of undercooling at the given temperature. The initial conditions are defined as follows

$$T|_{t=0}=T_0=\text{const.},\quad C|_{t=0}=C_0=\text{const.},$$
$$\mathbf{J}|_{t=0}=0,\quad \left.\frac{\partial C}{\partial t}\right|_{t=0}=0. \tag{3.1.5}$$

If a quench leads to rapid solidification, use of a local non-equilibrium approach to solute diffusion is warranted [14,15]. This approach requires a special condition at the diffusion front (i.e. at the front of the concentration profile which would move with the speed $V_D=(D/\tau_D)^{1/2}$, here τ_D represents the time of the diffusion relaxation) where a sharp concentration discontinuity occurs [14]. This sharp discontinuity at the diffusion front is taken into account by distinguishing the fluxes $\mathbf{J}_+$ and $\mathbf{J}_-$, and concentrations C_+ and C_- at: (1) the right-hand-side, and (2) the left-hand-side of the diffusion front, respectively. This leads to a boundary condition at the diffusion front "DF" in the following form:

$$(\mathbf{J}_+-\mathbf{J}_-)|_{DF}=V_D(C_+-C_-)|_{DF}\mathbf{n}, \tag{3.1.6}$$

where $\mathbf{n}$ is a normal unit-vector directed along the propagation of the concentration profile.

3.2. Idealizations

The following idealizations of the modeling of the solidification process were accepted:

1. Molten metal is considered as chemically inert, binary, non-eutectic alloy, i.e. the phase change is considered as a solidification into the solid solution (alpha phase) only. The nominal composition of the Si in the alloy at the onset of quench is assumed to be in the range between the initial and the

corresponding liquidus concentration at a given temperature, hence an undercooling is present.
2. The system is considered as a non-isothermal, two-phase system under the constant pressure.
3. Convective mechanisms are neglected.
4. All thermo-physical properties are assumed as constant.
5. Solute diffusion in liquid is non-Fickian.
6. Solute diffusion during quench in solid is neglected.

Idealization 1 is elaborated already within the context of the discussion of empirical evidence in Section 3.1, consult also [2]. The most important aspect of real conditions prior to solidification is a presence of Si diffusion across the clad–substrate interface and dissolution of the substrate at the interface (both prior to quench), thus leading to undercooling at the given temperature at the onset of solidification. It should be indicated that the concentration difference between the liquidus and the nominal values at a given temperature for the whole range of experimental conditions presented in Fig. 7, [2] (i.e., between 873 and 893 K) is in the range between 0% and 2.2%. As indicated in [13] the dissolution may reduce the Si concentration in the melt by up to 3.2% at 893 K with a smaller decrease at lower temperatures. So, in this study, the nominal concentration of Si in melt prior to quench is assumed to be within this margin to account for: (1) first an increase in Si concentration during melting (toward liquidus), and then (2) decrease of Si concentration during the dwell prior to quench, due to diffusion and dissolution at the substrate interfaces.

Idealization 5 introduces a non-Fickian mechanism of solute diffusion and gives evidence that the solute propagates with a finite diffusive speed V_D. As is well known, Fick's first law does not introduce in the model this finiteness, and it can be applied when the velocity of the process evolution is much smaller than the diffusive speed. In the case of rapid solidification, i.e. when the solidification speed can be of the order of magnitude (or even greater than the order of magnitude) of the diffusion speed in the bulk phase, i.e. $V \sim V_D$, one needs to take into account the finiteness of the solute diffusive propagation. In such a case, the connection between the concentration gradient and the diffusion flux will be defined not as an instant, but as inter-related by a relaxation law [7,16]. Taking the finiteness of the solute propagation into account promotes the possibility that a high-rate solidification can be modeled. Thus, in the present model, regardless of an apparently small solidification velocity (Fig. 9, [2]), the finiteness of the solute diffusive propagation is taken into account. For the Al + Si system under consideration, the value of V_D can be calculated by using Eqs. (3) and (4) from [16] (see Table 1 as well).

3.3. Governing equations

The set of governing equations for rapid solidification case developed in [14,17] must be extended for the non-isothermal solidification as considered here. By introducing the heat diffusion equation, the governing equations used in the present modeling are as follows [18]

$$\kappa \frac{\partial T}{\partial t} = \nabla \cdot (\lambda \nabla T) + Q \frac{\partial G}{\partial t}, \tag{3.3.1}$$

$$\frac{\partial}{\partial t}[(1-G)C_L + kGC_L] + \nabla \cdot \mathbf{J} = 0, \tag{3.3.2}$$

$$\tau_D \frac{\partial \mathbf{J}}{\partial t} + \mathbf{J} + D(1-G)\nabla C_L = 0, \tag{3.3.3}$$

$$\frac{\partial G}{\partial t} = \nabla \cdot [(1-G)\mathbf{V}], \tag{3.3.4}$$

$$C_S = kC_L. \tag{3.3.5}$$

Here C_L and C_S are the concentrations of solute in the liquid and the solid respectively, and $0 \leqslant G \leqslant 1$ is the solid fraction in a local volume of the system.

Eq. (3.3.2) describes the mass balance in the local volume of the two-phase mushy zone. Eq. (3.3.3) describes a modified Fick's law in a linear approximation (which takes into account a relaxation of the solute diffusion flux **J**). At low velocities of solidification, $V \ll V_D$, $\tau_D \to 0$, and Eq. (3.3.3) transfers into the classical Fick's law, i.e., $\mathbf{J} = -D(1-G)\nabla C_L$, where V is the projection of the solidification velocity vector **V** on the normal vector ***n*** to the interface. That is true for a description of the local equilibrium mass transfer in a two-phase mushy zone for the solidification of a binary system [15]. At high velocities, $V \sim V_D$ the relaxation term $\tau_D \partial J/\partial t$ in Eq. (3.3.3) qualitatively changes the mechanism of mass transfer. Specifically, as has been analyzed in [7], with taking into account the relaxation of the solute diffusion flux **J**, the concentration profile does not occur, and a chemically partitionless solidification process proceeds with $V \geqslant V_D$.

Eq. (3.3.4) describes evolution of the solid volume fraction G (see for details of the derivation and the features of this equation in Ref. [15]). Concentration difference at the interface involving Eq. (3.3.5) is dependent on the non-equilibrium solute partitioning parameter k which is a function of the velocity V.

In order to take into consideration the non-equilibrium solidification, a "temperature-concentration–velocity" relationship must be introduced (see, e.g., Ref. [19] and references therein). This relationship can be considered as being identical to the velocity dependent Gibbs–Thomson equation for a binary system. This equation infers:

$$T_I = T_A + mC_L + \left[\Gamma(\theta) + \frac{\partial^2\Gamma(\theta)}{\partial\theta^2}\right]K - V/\mu(\theta), \quad (3.3.6)$$

where θ is the angle between the normal to the interface and the z-axis. Together with Eq. (3.3.5), the expression given by Eq. (3.3.6) defines the temperature T_I at the solid–liquid interface as a function of the non-equilibrium chemical composition C_L. From Eq. (3.3.6) a non-linear equation for V is obtained in the form

$$V = \mu(\theta)[\Delta T - \Delta T_C(V) - \Delta T_N(V) - \Delta T_R - \Delta T_T], \quad (3.3.7)$$

where $\Delta T = T_A + m_e C_0 - T_0$ represents the total initial undercooling, as discussed in [2], and the respective definitions of the various undercooling contributions were given in Table 2 [2]. In Eqs. (3.3.6) and (3.3.7) the functions of the surface tension $\Gamma(\theta)$ and interfacial kinetics $\mu(\theta)$ are given by the expressions

$$\Gamma(\theta) = \Gamma_0[1 + \varepsilon_\Gamma \cos 4(\theta - \theta_\Gamma)],$$
$$\mu = \tilde{\mu}[1 - \varepsilon_\mu \cos 4(\theta - \theta_\mu)], \quad (3.3.8)$$

which are true for the fourth-fold symmetry of the growing crystal. Here ε_Γ and ε_μ are the anisotropy parameters ($\varepsilon_\Gamma, \varepsilon_\mu \ll 1$), and θ_Γ and θ_μ are the angles between the direction of growth and directions along which the functions $\Gamma(\theta)$ and $\mu(\theta)$ are minimal.

As is known, an introduction of stochastic parameters, i.e. the fluctuations in a deterministic model, allows one to model the same complex patterns that were observed. Taking into account the fluctuations in the growth pattern by using stochastic noise at the interface, we adopt the kinetic coefficient $\tilde{\mu}$ in Eq. (3.3.8) in the form as follows:

$$\tilde{\mu} = \mu_0[1 + \delta\eta(t, x, z)], \quad (3.3.9)$$

where $\delta \geqslant 0$ represents the noise amplitude, $\eta(t, x, z)$ is a random number uniformly distributed in $[-1; 1]$ at the solid–liquid interface at moment t. With $\delta > 0$, Eq. (3.3.7) implies a local difference in the interface velocity V. To calculate the mean curvature K (note $\Delta T_R = -\Gamma K$) at any point of the interface where $0 < G < 1$, one can assume the following relationship:

$$K = \frac{N_s - N_f}{2N_0 R}. \quad (3.3.10)$$

In Eq. (3.3.10) the following designations are accepted: N_s is the solid fraction of G at all sites of a growing crystal within a circle of a diameter $2R$; N_f is the solid fraction of G corresponding to a planar interface; finally, N_0 is the total number of sites in the circle.

4. Modeling of the dendritic growth

The main problem to be solved in handling the system of Eqs. (3.3.1)–(3.3.5) is related to the nature of the equations of the solute (3.3.2) and (3.3.3), and heat diffusion (3.3.1). The key issue involves significantly different time–space scales of the solute and heat diffusion. In other words, the values of the diffusion coefficient and thermal diffusivity imply corresponding time–space scales that differ from each other by an order of magnitude of 10^4 for the alloys under consideration, see Table 1. To solve these equations simultaneously and without a special approach to the computational algorithm would probably be impossible. Such an algorithm, and the accompanied special computational grids for the solution of these equations, will be proposed in [18], and were used extensively in this work.

4.1. Computational algorithm and the numerical approximation

The detailed computational scheme for solution of the non-Fickian solute diffusion problem in isothermal solidification, Eqs. (3.3.2) and (3.3.3), is given in Ref. [17]. To handle the significant difference between physical length scales of heat and mass transfer (heat and solute diffusion) in a non-isothermal problem, an efficient algorithm for the simultaneous solution of heat and mass transfer equations, Eqs. (3.3.1)–(3.3.3) has been developed. The key approach used by this algorithm is to solve the equations of heat transfer (3.3.1) and mass transfer (3.3.2) and (3.3.3) separately by using different lattices along with the exchange of the computational data between them [18]. The simultaneous solution of the heat and mass transfer equations in a non-isothermal solidification problem was realized by this algorithm thanks to an acceleration of the calculation under the well-distributed memory resources of a computer.

During the modeling of the solidification within the calculated domain, data are stored in a separately created binary file. Within this file, all of the computed data for the series of pertinent functions (such as G, C, T, etc.) are saved for every time step of modeling. For each time step, a plot is formed defining the distribution of (a) the fraction of the solid phase, (b) concentrations of the solute (Si) within both liquid and solid phase, and (c) temperature within the calculated domain. The algorithm and numerical scheme have been constructed for two different computational grids, i.e. separately for the thermal grid and the solute diffusion grid. Using such a multigrid method provides for an exchange of the dynamical data between these grids in accordance with the relation of the characteristic time scale and lengths for heat and mass transfer.

Under the present experimental conditions we were able to secure relatively small undercoolings and not too large growth velocities. Therefore, we have assumed in our modeling that the crystal growth shapes are determined mainly by the undercooling and anisotropy of the surface energy. In addition to material's parameters

given in Table 1, we have taken the following parameters for Eqs. (3.3.6)–(3.3.8): $\varepsilon_\Gamma = 0.01$, $\varepsilon_\mu = 0$, $\theta_\Gamma = 0$, and $\theta_\mu = 0$. In order to avoid grid anisotropy (which may have an influence on results of the modeling) we applied a special numerical procedure. The algorithm used can be briefly described as follows (it will be discussed in more details and with specific tests in [18]). First, we have taken into account the well-known fact that the grid selection influences the growth form due to various orientations of elementary volumes with respect to the vector of the growth velocity V (defined by the vector orthogonal to the solid–liquid interface). Second, within each elementary volume, we have computed the solid–liquid contour as a function of the angle between the velocity V and its projection on the x-axis and z-axis. And, third, for the computation of the solid fraction G in Eq. (3.3.4), we have taken into consideration both the growth velocity and length of the contour of the solid–liquid interface within each elementary volume. In such a case, the vector V defines an advancement of the interface and its growth direction, but the function of the contour length takes into account the orientations of every point at the interface with regard to origin(s) and prevents the grid anisotropy. Such algorithm significantly decreases the influence of the grid anisotropy on the crystal growth leading to physically isotropic structures which exhibit the tip splitting with isotropic properties of the solid–liquid interface.

4.2. Crystal pattern formation modeling

In the modeling, we have used the material parameters given in Table 1. Results for the calculated domain modeling for undercoolings of 14 K and 4 K and nominal concentration of 6.9 at.% are presented in Fig. 2. The dimensionless amplitude δ of the stochastic noise in modeling of the growth kinetics is 0.05. The total calculated domain is of the size of 100×300 μm, but the domain presented visually in Fig. 2 is of the size of 100×100 μm only. One pixel in Fig. 2 is equal to $320 \times a_0 = 0.16$ μm (where a_0 is the size of the interatomic distance, Table 1.) In Table 2, some additional data regarding the performed calculations are compiled.

It should be noted that for both calculations presented in Fig. 2, the interval of the physical time required for solidification is not larger than 0.03 s. Accordingly, the maximum of a temperature decrease at the boundaries 1 and 2, see Fig. 1, is 2.7 K, relative to T_0 for the cooling rates of 4 K/s and 7 K/s (see the color scales for Fig. 2). One can see that at the tip of a dendrite the temperature has been increased (due to release of the heat of solidification) with a great difference between the cases with different undercoolings: the temperature change for the case of solidification with $\Delta T = 14$ K is approximately two times greater than for the case of solidification with $\Delta T = 4$ K) (see Table 2). This fact is due to a more rapid crystal growth and more intensive release of the latent heat at the dendritic tip for the case of solidification with $\Delta T = 14$ K.

For two different undercoolings one obtains qualitatively different crystal structures during solidification. For $\Delta T = 14$ K, one gets the single dendrite which is growing from the initial substrate and with the developed dendritic ensemble behind it characterized with much smaller growth velocity (Fig. 2). For $\Delta T = 4$ K one gets the growth of a dendritic ensemble (Fig. 2). In order to explain this difference in selected structures we applied an analysis of linear stability of Mullins and Sekerka (MS) [19] as a first approximation. We assume that perturbations at the planar interface during solidification under the presented conditions during brazing were generated a priory, i.e., not developed as a consequence of the existence of the gradients of silicon concentration and the imposed undercooling at the interface. One may evaluate the (in)stability at the interface by using an expression for the stability wavelength λ_S below which the perturbations at the interface are stable as given by MS, i.e.,

$$\lambda_S = b_0 \left(\frac{D\Gamma_0}{V_P |m_e| (1 - k_e) C_0} \right)^{1/2}, \tag{4.2.1}$$

where V_P is the velocity of the planar interface, and b_0 is a dimensionless fitting parameter which is close to unity. For computations of λ_S versus V_P we have used the material's parameters from Table 1. The results of computations are shown in Fig. 3 for two undercoolings. As it can be seen from the figure, the planar interface is unstable in both considered cases of solidification. Therefore, the difference in a selection of the dendritic pattern shown in Fig. 2 *is not* in initial interface instability but it should be attributed to the pattern selection at the latest stages of the solidification process.

The results of the calculations for a range of nominal concentrations between 5.5 and 8.5 at.% (see Table 1) are illustrated in Fig. 4. As can be seen, a clear pattern selection of a dendrite structure is again more noticeable for a larger undercooling.

5. Analysis and discussion

This research has provided an evidence that in the brazing process of an Al–Si system exposed to CAB inert atmosphere the initial undercooling may have the significant influence on morphology, if Si depletion prior to quench is present. Such situation is inherent to cases of re-solidification of micro-layers of Si rich Al alloy over the Si lean substrate, as is the case of a typical brazing process involving aluminum brazing sheets.

A significant improvement of the model would be achieved by an extension of the present solid solution

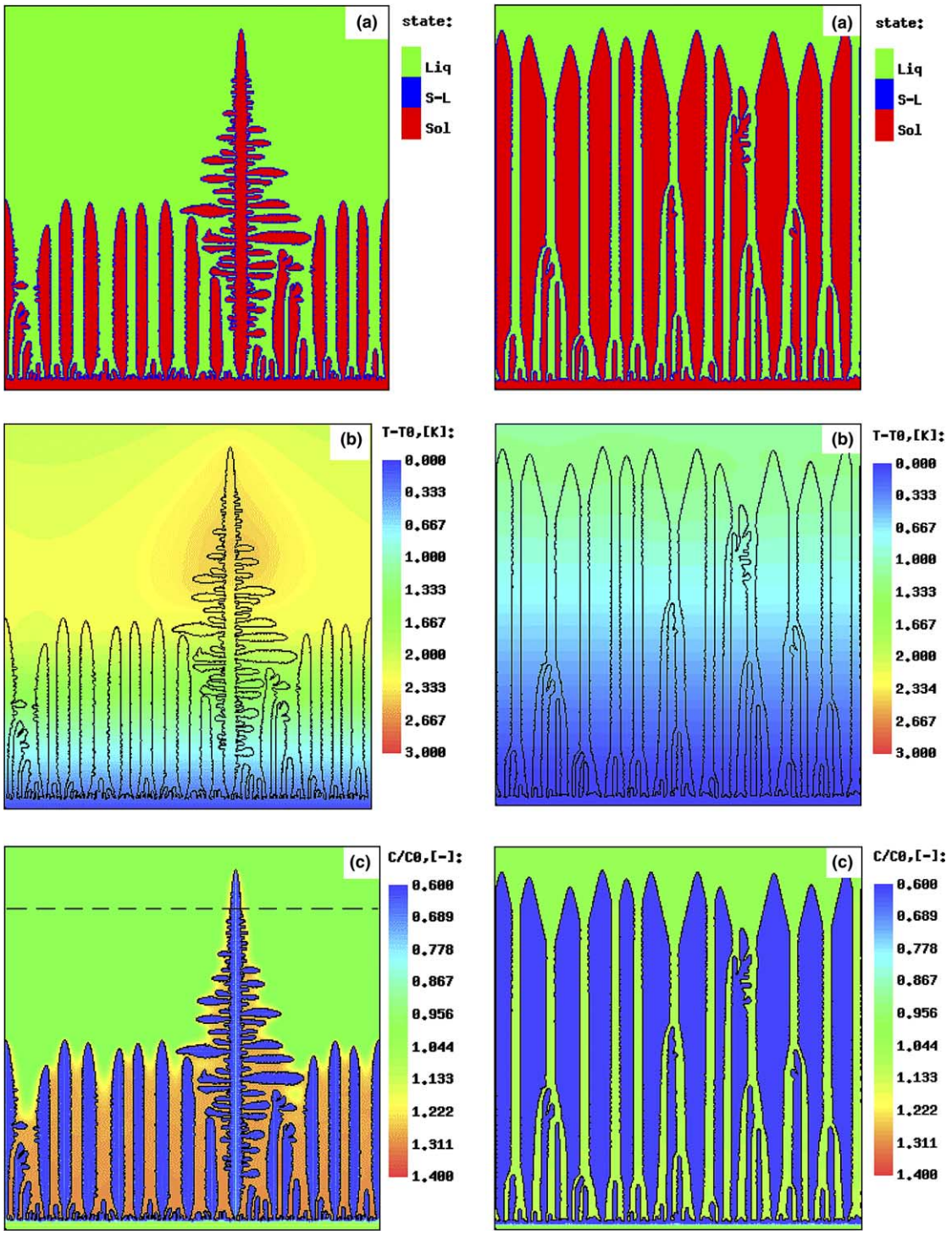

Fig. 2. Simulation of a solidification microstructure. Left column: Al + Si solid solution quenched following the cooling curve at 873 K as presented in Fig. 3b [2]. Undercooling is equal to $\Delta T = 14$ K, (a) a state of phases in the solidifying domain; (b) distribution of temperature; (c) distribution of Si concentration in the liquid phase and solid crystal phase. The dashed line in (c) indicates the location that corresponds to Fig. 5 concentration profile (numerical data). Right column: Al + Si solid solution quenched following the cooling curve at 883 K as presented in Fig. 3b [2]. Undercooling is equal to $\Delta T = 4$ K.

Table 2
Description of the large domain modeling of solidification microstructures for experimental results presented in Fig. 1 [2]

Modeling presented in Fig. 2	Item	Microstructure presented in Fig. 1a [2]	Microstructure presented in Fig. 1b [2]
General info	Size of calculated domain: 100×300 μm	Calculations are made in the laboratory reference frame	Calculations are made in the laboratory reference frame
	Initial undercooling (K)	14	4
	Cooling rate (K/s)	7	4
	Calculated time interval (s)	4.66×10^{-3}	2.83×10^{-2}
Inset (a)	Phase-state distribution (crystal, liquid, and the solid–liquid interface)	Single dendrite	Dendritic ensemble
Inset (b)	Temperature distribution (K)	$0.0 < T - T_0 < 2.67$	
Inset (c)	Concentration of Si distribution in the melt (–)	$1.04 < C/C_0 < 1.13$	
	Concentration of Si distribution in the solid (–)	$0.60 < C/C_0 < 0.78$	
Velocity	At the tip of the more developed dendrite (mm/s)	18.65	
Temperature increase with respect to T_0	At the tip of the more developed dendrite (K)	2.23	0.33

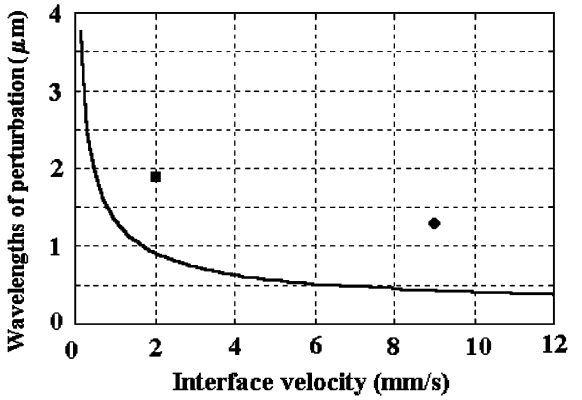

Fig. 3. Prediction of the Mullins–Sekerka theory [19] for the critical wavelengths of perturbation on a planar interface (solid curve) in comparison with the present numerical data (solid circle is for $\Delta T = 14$ K and solid square is for $\Delta T = 4$ K). The curve shows the demarcation line above which the planar interface is unstable. Modeling data points were extracted on the initial stages of the interface instability.

solidification model to the dendritic/eutectic alloy solidification. In Fig. 5 the difference between the model and the actual conditions is indicated in terms of the dimensionless concentration distribution of the solute in and around the dendrite stem for: (1) the numerical model, see Fig. 2c, left column, and (2) experimental data [2]. The dashed line in Fig. 2c indicates the position of a cross-section through the liquid and solid phases from which the data for Fig. 5 are taken. The experimental data points indicated in Fig. 5 were obtained from the electron probe microanalyzer (EPMA) linear scans made through an alpha phase grain located within the joint zone (solid state) [12]. The numerical values are dimensionalized as follows: (1) the length coordinate is scaled by the corresponding characteristic dimension of the solid solution/alpha phase stem/grain, so that its region is between 0 and 1 on the abscissa, for both numerical and experimental data, and (2) the concentration level is scaled by the solute concentration in the melt (assumed to be equal to the nominal Si concentration, see Table 1).

As can be seen from Fig. 5, the general behavior of concentration obtained from the modeling data is the same as was obtained from experimental data. Quantitatively, a disagreement between experimental measurements and modeling data occurs in vicinity of the boundary of the dendrite stem and surrounding matrix. These differences can be explained by the presence of eutectic microstructures with higher concentration of silicon in the experiment during and after solidification. The present model does not include the eutectic precipitation; however, it still provides basic qualitative agreement with the experimental data, Fig. 5. Within the stem of a dendrite, the computed behavior of the Si concentration is sufficiently good compared with the experimental data, both qualitatively and quantitatively. Note that Si concentration is determined within the error margin of at least 0.05 wt.%, [12]. However, it should also be noted that both in model calculations and experimental data, the concentration within the core of dendrite has a clear tendency to a local increase (see Fig. 5, at the abscissa equal to 0.5). This feature can be explained by higher trapping of silicon during the non-steady, transient regime of the solidification when the core of the dendrite stem is forming.

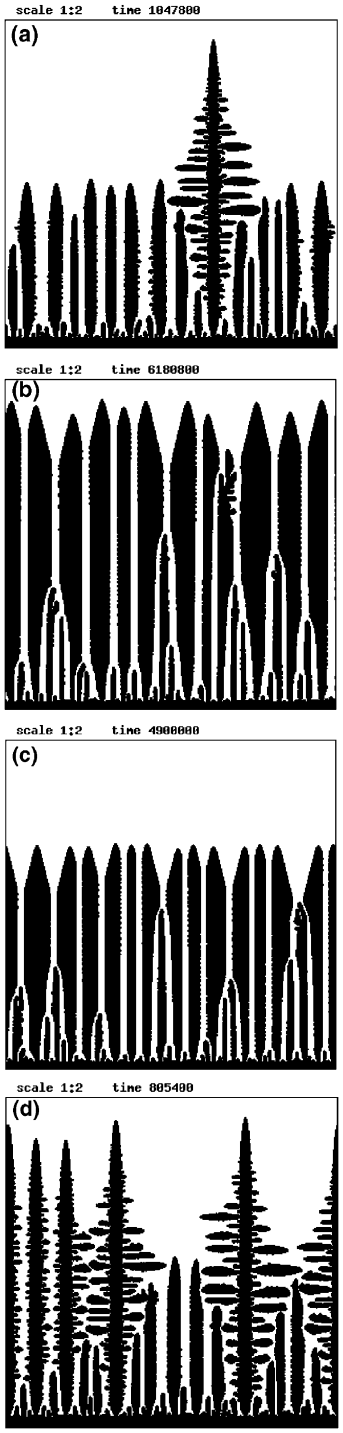

Fig. 4. Simulation of a solidification microstructure, Al + Si solid solution formation from an equivalent melt at nominal concentrations of 6.9 (a, b), 8.5 (c) and 5.5 at.% Si. The quench is from 873 K (a, c) and 883 K (b, d), [24].

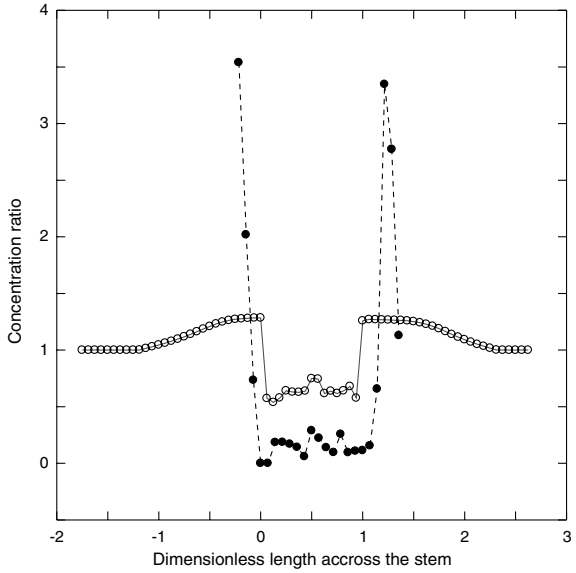

Fig. 5. The concentration profiles for Si across a solid solution/melt cross-section. Numerical data marked by a solid line and open circles. Experimental data indicated by solid points and dashed line.

Some questions raised in the course of this investigation still await satisfactory answers. For example, it may be very useful for a further model development to clarify why the structure presented in Fig. 2. left column, exhibits a forest of cells and dendrites behind the unique selected dendrite. In contrast to the modeling data, Fig. 2, the actual experimental structure shown in Fig. 1a, [2], does exhibit a free-dendritic pattern in the alloy. One possible contributing factor to this discrepancy (note that in some experiments more than a single dendrite is present even for lower temperatures at the onset of quench, but certainly not so numerous as at the higher peak temperatures), may be that after selection of a single dendrite from the dendritic forest (due to pattern selection mechanism occurring at the latest stages of solidification, see, e.g. Ref. [20]), a remelting mechanism may come into action (due to a release of the latent heat within the solidifying domain). To verify this idea, it is necessary to provide detailed modeling of a sequence of both processes, i.e., solidification and melting.

Finally, an important issue related to the modeling approach adopted in this study deserves an additional comment. We have taken into account the role of the crystalline anisotropy in crystal growth. Analytically, this influence can be considered with using the solvability theory [21,22]. The solvability conditions are now well defined only for pure one-component systems where the anisotropy of surface energy and/or the growth kinetics is included by a model of dendritic growth [22]. Very recently, the conditions of solvability have

been established in pure systems for both the anisotropy of surface energy and growth kinetics of the dendritic interface in comparison with the predictions of the phase-field model [23]. So, for the considered Al–Si alloy, we introduced the anisotropy of the surface energy into the model (see Section 4.1 and also equations in Section 3.3 in which we take into account the finite anisotropy strength ε_Γ of the surface energy and the zero value for the anisotropy strength ε_μ of the kinetics) for a prediction of the kinetics of the dendritic growth.

In the developed numerical model (see Section 3.3), the *anisotropy of the grid* has been reduced drastically to resolve the problem numerically with taking into account both anisotropic properties of the interface. The simultaneous solution of two very different-scaled processes (i.e., heat diffusion and solute diffusion) required significant computational time and sizable computer's memory (for examole, we have used a node of a HP N-4000 supercomputer having 8 PA-RISC 8500 @ 440 MHz with 8GB RAM of memory).

6. Conclusions

For detailed 2D modeling we have used the model of local non-equilibrium solidification and developed it within the framework of the two-phase mushy zone. The present model of the two-phase mushy zone for the non-isothermal solidification extends the previously developed isothermal model of the solidification within the mushy zone. The developed system of model equations has been solved numerically and the model predictions were compared with the empirical findings related to dendritic microstructures for cases of relatively sluggish solidification kinetics.

From the results of modeling it can be concluded that the initial undercooling ΔT from which the solidification in the alloy starts to evolve is the main governing parameter of the pattern evolution in the solidification process during aluminum brazing. We identified a transition from the ensemble of dendrites (compare Fig. 1b [2] and Fig. 2) to the unified free dendrite (compare Fig. 1a [2] and Fig. 2) respectively. The reason why such a transition can occur might be seen in (i) rapid decreasing of undercooling around the interface for $\Delta T = 14$ K and a more developed constitutional undercooling around the interface for $\Delta T = 4$ K, and (ii) the existence of a competition between the solute diffusion and the surface tension during the transient period of solidification when the selection of wavelengths at the latest stages of solidification takes place.

Acknowledgments

The National Science Foundation has provided support through the NSF Grant DMI-9908319, monitored by Dr. Delcie Durham and Dr. Julie Chen. P.K. Galenko acknowledges support from the Alexander von Humboldt Foundation through the research program no. IV RUS 1068584. An early version of some aspects of this research was presented at the 7th Int. Conference on Brazing, LOT 2004 in Aachen, Germany, [24].

References

[1] B.P. Zellmer, N. Nigro, D.P. Sekulic, Numerical modeling and experimental verification of the formations of 2D and 3D brazed joints, Modelling Simul. Mater. Sci. Eng. 9 (2001) 339.
[2] D.P. Sekulic, P.K. Galenko, M.D. Krivilyov, L. Walker, F. Gao, Dendritic growth in Al–Si alloys during brazing. Part 1: Experimental evidence and kinetics, Int. J. Heat Mass Transfer, in press.
[3] Daming Xu, Qingchun Li, Numerical method for solution of strongly coupled binary alloy solidification problems, Numer. Heat Transfer Part A 20 (1991) 181–201.
[4] J.P. Delplanque, E.J. Lavernia, R.H. Rangel, Multidirectional solidification model for the description of micro-pore formation in spray deposition processes, Numer. Heat Transfer Part A 30 (1996) 1–18.
[5] W.D. Bennon, F.P. Incropera, Numerical analysis of binary solid–liquid phase change using a continuum model, Numer. Heat Transfer 13 (1988) 277–296.
[6] A.V. Kuznetsov, K. Vafai, Comparison between the two- and three-phase models for analysis of porosity formation in aluminum-rich castings, Numer. Heat Transfer Part A 29 (1996) 859–867.
[7] P. Galenko, S. Sobolev, Local nonequilibrium effect on undercooling in rapid solidification of alloys, Phys. Rev. E 55 (1997) 343–352.
[8] P.K. Galenko, D.A. Danilov, Local nonequilibrium effect on rapid dendritic growth in a binary alloy melt, Phys. Lett. A 235 (1997) 271–280.
[9] P.K. Galenko, D.A. Danilov, Model for free dendritic alloy growth under interfacial and bulk phase nonequilibrium condition, J. Cryst. Growth 197 (1999) 992–1002.
[10] D.P. Sekulic, F. Gao, H. Zhao, B. Zellmer, Y.Y. Qian, Prediction of the fillet mass and topology of aluminum brazed joints, Welding J., Res. Suppl. 83 (3) (2004) 102s–110s.
[11] H. Zhao, D.P. Sekulic, Modeling of the influence of a microstructure scale on the re-solidification of micro-layers of a molten aluminum alloy. Proc. Of the Fourth Int. Symposium on Scale Modeling ISSM-IV, Cleveland, Ohio, NCRM-NASA Glen Research Center, 2003, pp. 291–301.
[12] F. Gao, Z. Hui, D.P. Sekulic, Y. Qian, L. Walker, Solid state Si diffusion and joint formation involving aluminum brazing sheet, Mater. Sci. Eng. A 337 (2002) 228–235.
[13] R.A. Woods, I.B. Robinson, Flow of aluminum dip brazed filler metals, Welding J., Res. Suppl 53 (1974) 440s–445s.
[14] P.K. Galenko, M.D. Krivilyov, Model for isothermal pattern formation of growing crystals in undercooled binary alloys, Modelling Simul. Mater. Sci. Eng. 8 (2000) 67–79.
[15] P.K. Galenko, V.A. Zhuravlev, Physics of Dendrites, World Scientific, Singapore, 1994.

[16] P. Galenko, Extended thermodynamical analysis of a motion of the solid–liquid interface in a rapidly solidifying alloy, Phys. Rev. B 65 (2002) 144103-1–144103-11.
[17] P.K. Galenko, M.D. Krivilyov, Modelling of crystal pattern formation in isothermal undercooled alloys, Modelling Simul. Mater. Sci. Eng. 8 (2000) 81–94.
[18] P.K. Galenko, M.D. Krivilyov, to be published.
[19] W. Kurz, D.J. Fisher, Fundamentals of Solidification, third ed., Trans Tech Publications, Aedermannsdorf, 1992.
[20] F. Liu, N. Goldenfeld, Generic features of late-stage crystal growth, Phys. Rev. A 42 (1990) 895–903.
[21] D.A. Kessler, J. Koplik, H. Levine, Pattern selection in fingered growth phenomena, Adv. Phys. 37 (1988) 255–339.
[22] E.A. Brener, V.I. Melnikov, Pattern selection on two-dimensional dendritic growth, Adv. Phys. 40 (1991) 53–97.
[23] J. Bragard, A. Karma, Y.H. Lee, M. Plapp, Linking phase-field and atomistic simulations to model dendritic solidification in highly undercooled melts, Interf. Sci. 10 (2-3) (2002) 121–136.
[24] M.D. Krivilyov, P.K. Galenko, D.P. Sekulic, Modeling of Al–Si alpha-phase crystal pattern formation during aluminum brazing, DVS Berichte 231 (2004) 126–129.
[25] M. Rappaz, W.J. Boettinger, Acta Mater. 47 (1999) 3205–3219.
[26] T.B. Massalski (Editor-in-Chief), H. Okamoto, P.R. Subramanian, L. Kacprzak (Eds.), Binary Alloy Phase Diagrams, 2nd ed., vol. 1, ASM International, USA, 1996.